Article

Na$_2$Ti$_3$O$_7$@RF@Ag Heterostructures as Efficient Substrates for SERS and Photocatalytic Applications

Yu-Cheng Chang [1,*], I-Chun Lin [1], Ning-Chien Chin [1,2], Sin-Ei Juang [1,3] and Chia-Man Chou [4,5,6,*]

[1] Department of Materials Science and Engineering, Feng Chia University, Taichung 40724, Taiwan; a0931776422@gmail.com (I.-C.L.); a111079@mail.tsmh.org.tw (N.-C.C.); juang5251@cgmh.org.tw (S.-E.J.)

[2] Department of Orthopedics, Antai Tian-Sheng Memorial Hospital, Antai Medical Care Corporation, Pingtung 92842, Taiwan

[3] Department of Anesthesiology, Kaohsiung Chang Gung Memorial Hospital, Chang Gung University College of Medicine, Kaohsiung 83301, Taiwan

[4] Department of Surgery, Taichung Veterans General Hospital, Taichung 40705, Taiwan

[5] College of Medicine, National Yang Ming Chiao Tung University, Taipei 11221, Taiwan

[6] Department of Post-Baccalaureate Medicine, National Chung Hsing University, Taichung 40227, Taiwan

[*] Correspondence: yuchchang@fcu.edu.tw (Y.-C.C.); cmchou@vghtc.gov.tw (C.-M.C.)

Abstract: A multi-step procedure was effectively employed to synthesize innovative three-dimensional (3D) heterostructures encompassing sodium titanate (Na$_2$Ti$_3$O$_7$) nanowire cores, an intermediate resorcinol–formaldehyde (RF) layer, and outer silver (Ag) nanoparticle sheaths, referred to as Na$_2$Ti$_3$O$_7$@RF@Ag heterostructures. Initially, a one-step hydrothermal technique facilitated the direct growth of single-crystal Na$_2$Ti$_3$O$_7$ nanowires onto a flexible Ti foil. Subsequently, a two-step wet chemical process facilitated the sequential deposition of an RF layer and Ag nanoparticles onto the Na$_2$Ti$_3$O$_7$ nanowires at a low reaction temperature. Optimal concentrations of silver nitrate and L-ascorbic acid can lead to the cultivation of Na$_2$Ti$_3$O$_7$@RF@Ag heterostructures exhibiting heightened surface-enhanced Raman scattering (SERS), which is particularly beneficial for the detection of rhodamine B (RhB) molecules. This phenomenon can be ascribed to the distinctive geometry of the Na$_2$Ti$_3$O$_7$@RF@Ag heterostructures, which offer an increased number of hot spots and surface-active sites, thereby showcasing notable SERS enhancement, commendable reproducibility, and enduring stability over the long term. Furthermore, the Na$_2$Ti$_3$O$_7$@RF@Ag heterostructures demonstrate remarkable follow-up as first-order chemical kinetic and recyclable photocatalysts for the photodecomposition of an RhB solution under UV light irradiation. This result can be attributed to the enhanced inhibition of electron–hole pair recombination and increased surface-active sites.

Keywords: one-dimensional heterostructures; sodium titanate nanowires; resorcinol–formaldehyde; silver nanoparticle; surface-enhanced Raman scattering; rhodamine B; photocatalysts

1. Introduction

Surface-enhanced Raman scattering (SERS) greatly amplifies the Raman signals of analytes near enhancing materials [1,2]. Electromagnetic and chemical enhancements, particularly electromagnetic field amplification (localized surface plasmon resonance (LSPR)) and charge transfer, contribute to Raman signal enhancement [3–5]. This dual-path enhancement elevates SERS sensitivity to single-molecule levels while retaining Raman spectroscopy advantages [6]. The pivotal aspect of SERS lies in enhancing substrates, notably plasmonic substrates, with Ag and Au being the most efficient due to their inherent plasmonic properties [7–10]. The substrate's geometry, particularly the surface localization of nanostructures, is crucial for sustaining strong surface plasmon resonance (SPR), and the surface chemistry of these nanostructures significantly influences the intensity of SPR peaks [11–15]. At present, combining semiconductor nanostructures with noble

metal nanoparticles, known as metal–semiconductor heterostructures, offers a promising approach to creating three-dimensional (3D) LSPR structures to enhance SERS substrates' detection sensitivity and uniformity [16–21]. These heterostructures can serve as recyclable SERS substrates through the photocatalytic degradation of target molecules under UV light irradiation and facilitate charge transfer pathways for Raman scattering enhancement [22–24]. Among semiconductor nanostructures, titanium dioxide (TiO_2) and zinc oxide (ZnO) nanostructures are popular due to their excellent photocatalytic activity when exposed to UV light, making them ideal SERS substrates [25–27]. Nevertheless, fewer studies explore the use of sodium titanate nanostructures in SERS and photocatalysis [28].

Sodium titanate ($Na_2Ti_nO_{2n+1}$, where $2 \leq n \leq 9$) has garnered considerable attention as a promising material due to its notable attributes: a high level of chemical inertness, non-toxicity, ion exchange capabilities, and cost-effectiveness [29–31]. This versatile substance finds applications in chemical absorption, photocatalysis, supercapacitors, and sodium-ion batteries [32–37]. Numerous synthesis methods have been employed to fabricate sodium titanate nanostructures [38–40]. The hydrothermal method has emerged as a preferred choice due to its simplicity and cost-effectiveness, making it widely used for obtaining a diverse range of nanostructures [35,41]. One-dimensional sodium titanate nanostructures adorned with Ag nanoparticles via an ion-sputtering technique have recently emerged as highly effective SERS substrates, showcasing exceptional detection sensitivity, stability, and uniformity [28]. This limitation stems from the necessity to conduct the deposition of Ag nanoparticles under high-vacuum conditions, which are energy-intensive and not environmentally friendly.

Prior investigations have often resorted to thermal evaporation or ion-sputtering techniques to achieve the uniform deposition of Au or Ag nanoparticles on one-dimensional semiconductor nanostructures to fabricate 3D SERS substrates [42–44]. These methods can effectively produce high-performance SERS substrates but fall short regarding energy savings and carbon reduction [45]. Moreover, the literature dedicated to the development of SERS substrates on one-dimensional semiconductor nanostructures through the application of a resorcinol–formaldehyde (RF) resin layer, a strategy aimed at diminishing the reliance on noble metal nanoparticles, has been relatively scant [46,47]. In earlier studies, resorcinol exhibited versatility by serving as a critical reactant in forming the RF layer and playing an essential role in passivating the surfaces of metal nanoparticles to prevent agglomeration [48,49]. Furthermore, resorcinol's capabilities extended to acting as a reducing agent, facilitating the conversion of metal salts into their nanoparticle counterparts [50,51]. This innovative approach promises effective SERS substrates and aligns with sustainability goals by reducing the carbon footprint associated with traditional high-vacuum methods.

This study details the fabrication of $Na_2Ti_3O_7$@RF@Ag heterostructures achieved through straightforward hydrothermal and wet chemical techniques, aiming to enhance their photocatalytic and SERS capabilities. The optimization of $AgNO_3$ and L-ascorbic acid volumes was explored to maximize SERS enhancement, specifically for detecting rhodamine B (RhB) molecules. The $Na_2Ti_3O_7$@RF@Ag heterostructures were thoroughly characterized to reveal their morphology, crystal structure, and chemical composition using microscopic and spectroscopic techniques. These heterostructures offer improved separation of photoelectron–hole pairs and increased surface-active sites, enhancing their photocatalytic efficiency and reusability. Additionally, the $Na_2Ti_3O_7$@RF@Ag heterostructures present an advantageous geometry for the uniform deposition of Ag nanoparticles, facilitating the creation of high-performance SERS and photocatalytic substrates.

2. Results and Discussion

Figure 1 presents a schematic representation of the fabrication process for cultivating $Na_2Ti_3O_7$@RF@Ag heterostructures. Initially, a straightforward hydrothermal technique was utilized to nurture $Na_2Ti_3O_7$ nanowires on a Ti foil at 220 °C for 5 h. Subsequently, a self-assembled APTMS ((3-Aminopropyl)trimethoxysilane) monolayer was employed to enhance the hydrophilic properties of $Na_2Ti_3O_7$ nanowires, allowing for the uniform

decoration of the RF layer [47]. Lastly, $Na_2Ti_3O_7$ nanowires coated with an RF layer, in conjunction with L-ascorbic acid, facilitated the reduction of Ag^+ to Ag, culminating in the formation of $Na_2Ti_3O_7$@RF@Ag heterostructures.
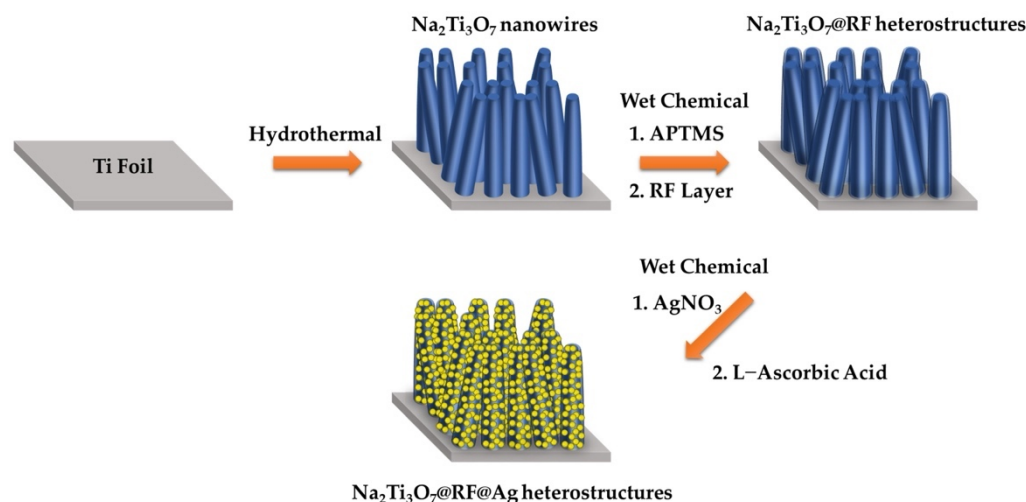

Figure 1. Synthetic scheme of the preparation of the $Na_2Ti_3O_7$@RF@Ag heterostructures.

Figure 2 illustrates the X-ray powder diffraction (XRD) patterns of the $Na_2Ti_3O_7$ nanowires, $Na_2Ti_3O_7$@RF heterostructures, and $Na_2Ti_3O_7$@RF@Ag heterostructures. The XRD patterns for the $Na_2Ti_3O_7$ nanowires (Figure 2a) exhibit distinct peaks at 2θ values of 24.3°, 28.5°, 48.5°, and 49.5°, corresponding to the (102), (111), (303), and (410) crystal planes of monoclinic-phase $Na_2Ti_3O_7$ (JCPDS Card No. 72-0148), respectively. Additionally, these peaks are observed at 2θ angles of 35.1°, 38.4°, 40.2°, 53.0°, 62.9°, 70.7°, 74.2°, 76.2°, and 77.4°, corresponding to the (100), (002), (101), (102), (110), (103), (200), (112), and (201) crystal planes of hexagonal-phase Ti (JCPDS Card No. 44-1294), respectively. Figure 2b shows the XRD pattern of $Na_2Ti_3O_7$@RF heterostructures of $Na_2Ti_3O_7$ nanowires without any distinctive peaks. Notably, the presence of Ag nanoparticles within the $Na_2Ti_3O_7$@RF@Ag heterostructures (Figure 2c) is evident from the faint peaks at 2θ values of 38.2°, 44.4°, 64.6°, and 77.6°, corresponding to the (111), (200), (220), and (311) crystal planes of cubic-phase Ag (JCPDS Card No. 87-0720). This outcome verifies the absence of impurities within the $Na_2Ti_3O_7$@RF@Ag heterostructures.

The FESEM morphology (Figure 3a) of the $Na_2Ti_3O_7$ nanowires reveals a high-density distribution of these nanowires that have grown across the entire surface of the Ti foil, displaying a random orientation. Figure 3b displays a FETEM image of a $Na_2Ti_3O_7$ nanowire featuring an intermediate diameter of approximately 105 nm. Additionally, Figure 3c reveals a selected area electron diffraction (SAED) pattern of a $Na_2Ti_3O_7$ nanowire, presenting a well-defined arrangement of single crystal dots. This single-crystal-dot array corresponds to the crystal structure of the $Na_2Ti_3O_7$ nanowire and aligns with the monoclinic $Na_2Ti_3O_7$ crystal phase (JCPDS Card No. 72-0148). The HRTEM image (Figure 3d) demonstrates an index lattice spacing of 0.314 nm, which agrees with the lattice spacing of the (111) plane of $Na_2Ti_3O_7$. In addition, the FETEM-EDS mapping images (Figure 3e) prove the homogeneous distribution of Ti, O, and Na elements in the nanowire. The calculated atomic percentages of the $Na_2Ti_3O_7$ nanowires from the FETEM-EDS mapping images reveal the following compositions: Na 7.9%, Ti 25.1%, and O 67%.

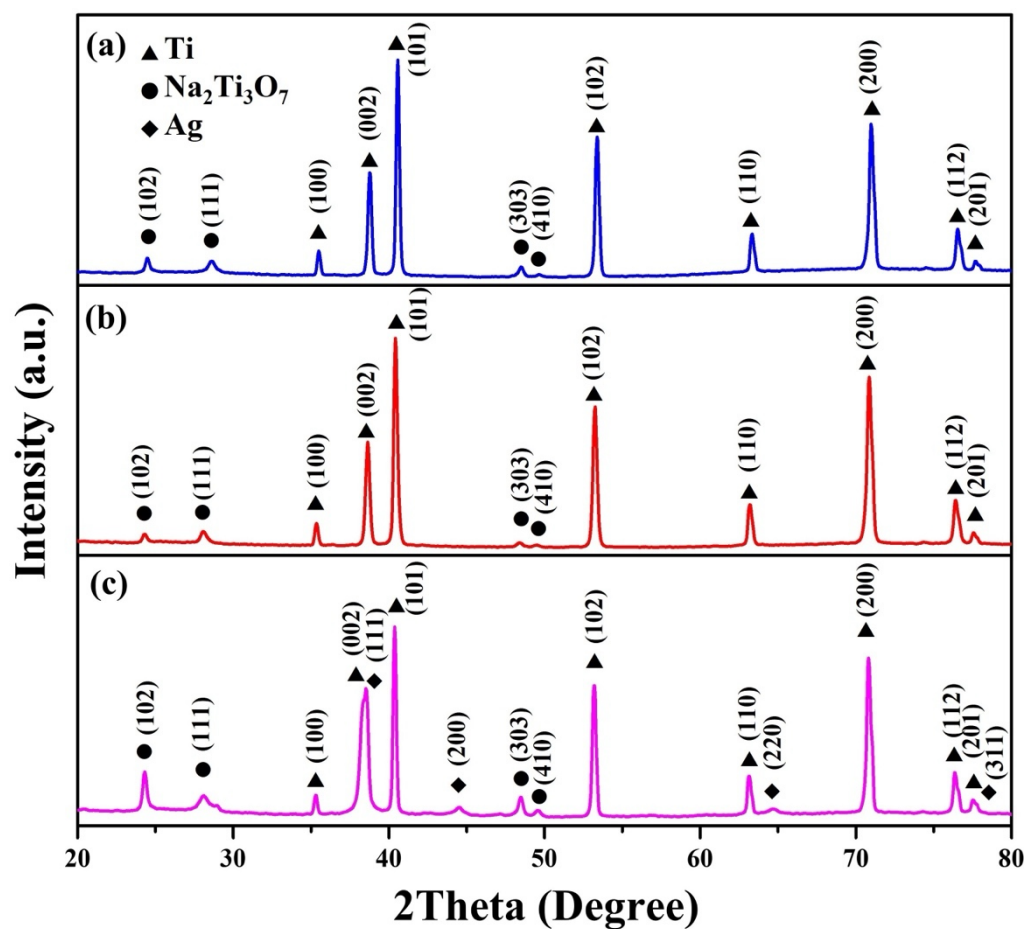**Figure 2.** XRD spectra of (**a**) $Na_2Ti_3O_7$ nanowires, (**b**) $Na_2Ti_3O_7$@RF heterostructures, and (**c**) $Na_2Ti_3O_7$@RF@Ag heterostructures.
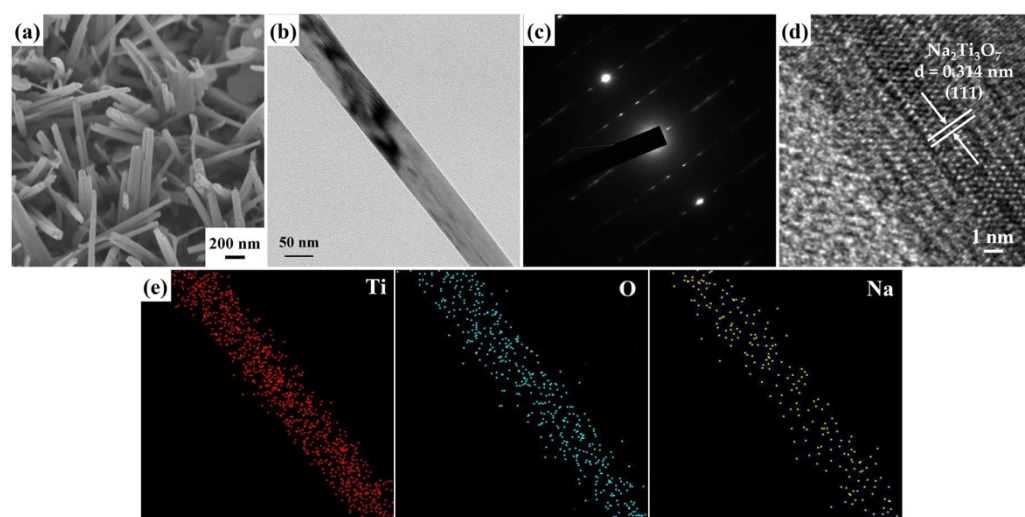

Figure 3. (**a**) A 45° tilt-view FESEM image of the $Na_2Ti_3O_7$ nanowires. (**b**) FETEM image, (**c**) SAED pattern, (**d**) HRTEM image, and (**e**) FETEM-EDS mapping image of a $Na_2Ti_3O_7$ nanowire.

Figure 4a reveals an FETEM image of a $Na_2Ti_3O_7$@RF heterostructure with a core–shell structure. Figure 4b shows an SAED pattern of a $Na_2Ti_3O_7$@RF heterostructure which only presents a single-crystal-dot array aligned with the monoclinic $Na_2Ti_3O_7$ crystal phase (JCPDS Card No. 72-0148). The HRTEM image (Figure 4c) reveals the presence of an approximately 4.02 nm thick amorphous RF layer decorated on the $Na_2Ti_3O_7$

nanowire. Additionally, a lattice fringe characterized by an interplanar spacing of 0.314 nm corresponds to the (111) plane of the monoclinic $Na_2Ti_3O_7$ crystal phase (JCPDS Card No. 72-0148). The FETEM-EDS mapping images (Figure 4d) still exhibit the heterostructure's homogeneous Ti, O, and Na distribution. This observation verifies that the presence of the RF layer on the $Na_2Ti_3O_7$ nanowire does not induce any alterations in the material's elemental composition.

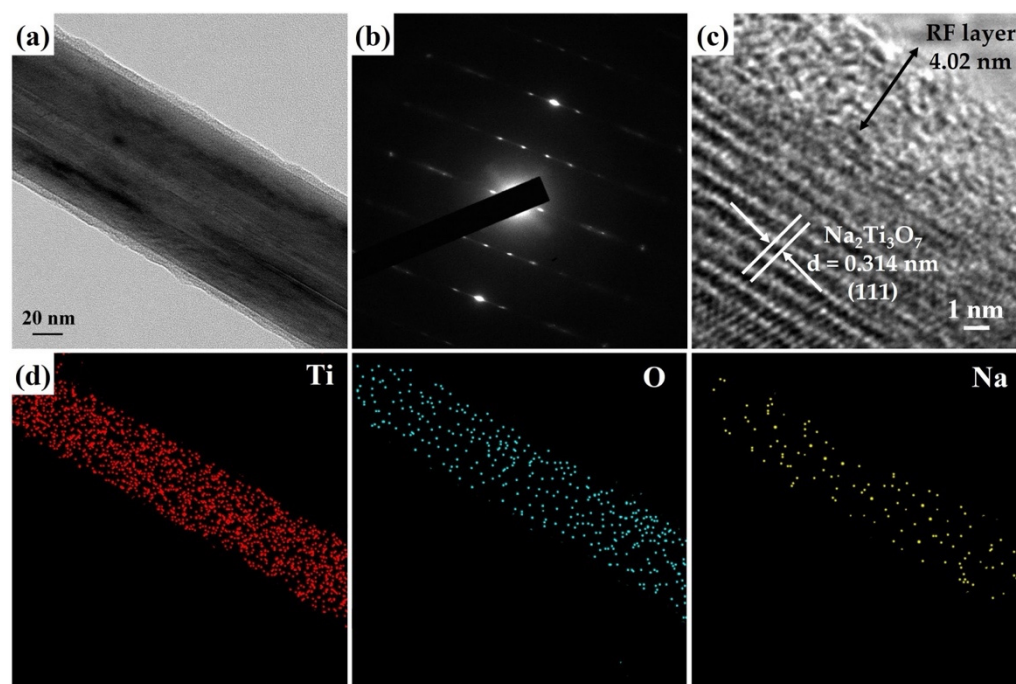**Figure 4.** (**a**) FETEM image, (**b**) SAED pattern, (**c**) HRTEM image, and (**d**) FETEM-EDS mapping image of a $Na_2Ti_3O_7$@RF heterostructure.

Figure 5a,b presents the FETEM images of a $Na_2Ti_3O_7$@RF@Ag heterostructure grown using 0.15 mL $AgNO_3$ and 3 mL L-ascorbic acid volumes. The FETEM images can reveal that the Ag nanoparticles' size is about 3–10 nm, and they are completely decorated on the $Na_2Ti_3O_7$@RF heterostructure. The SAED pattern (Figure 5c) of a $Na_2Ti_3O_7$@RF@Ag heterostructure displays a combination of a single-crystal-dot array and a polycrystalline ring. The presence of a single-crystal-dot array in the SAED pattern of $Na_2Ti_3O_7$@RF@Ag heterostructure corresponds to the crystalline structure of $Na_2Ti_3O_7$ nanowire, which aligns with the monoclinic $Na_2Ti_3O_7$ crystal phase (JCPDS Card No. 72-0148). This alignment indicates the well-preserved crystal structure of $Na_2Ti_3O_7$ even after the deposition of Ag nanoparticles. The Ag nanoparticles' distinctive appearance exhibited a concentric ring pattern, corresponding to the diffraction from the (111) plane of the cubic Ag crystal structure (JCPDS Card No. 87-0720). The HRTEM image of the $Na_2Ti_3O_7$@RF@Ag heterostructure (Figure 5d) shows two visible lattice fringes exhibiting an interplanar spacing of 0.235 nm which can be confidently attributed to the (111) lattice plane of the cubic Ag (JCPDS Card No. 87-0720). This observation underscores the successful deposition of cubic-phase Ag nanoparticles within the heterostructures. The FETEM-EDS mapping image (Figure 5d) provides valuable insights into the composition of the $Na_2Ti_3O_7$@RF@Ag heterostructure. This composition analysis reveals the presence of Ti, O, Na, and Ag elements within the $Na_2Ti_3O_7$@RF@Ag heterostructure, indicating the successful synthesis of this heterostructure through a two-step wet chemical process on the $Na_2Ti_3O_7$ nanowire.

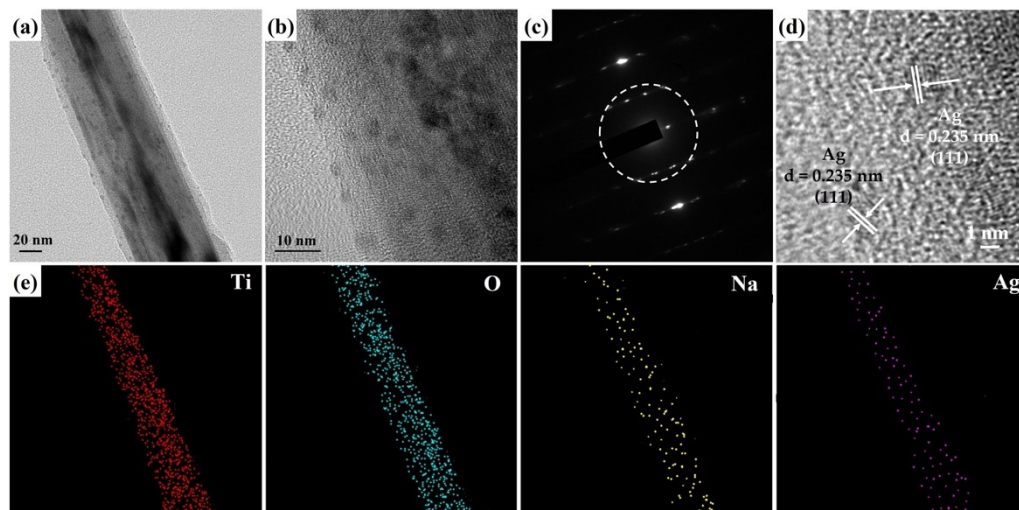**Figure 5.** (**a**,**b**) FETEM image, (**c**) SAED pattern, (**d**) HRTEM image, and (**e**) FETEM-EDS mapping image of a $Na_2Ti_3O_7$@RF@Ag heterostructure (0.15 mL of Ag NO_3 and 3 mL of L-ascorbic acid).

X-ray photoelectron spectroscopy (XPS) is a powerful tool for investigating the chemical states of elements in $Na_2Ti_3O_7$@RF@Ag heterostructures (0.15 mL $AgNO_3$ and 3 mL L-ascorbic acid volumes), providing valuable insights into surface chemistry. The XPS survey spectrum (Figure 6a) shows the existence of Na, Ti, C, O, N, and Ag in the $Na_2Ti_3O_7$@RF@Ag heterostructures. The high-resolution (HR) XPS spectrum of Na 1s (Figure 6b) exhibits a peak at 1071.4 eV, confirming the valence state of Na as +1 [52,53]. The presence of Ti^{4+} species is confirmed by Ti 2p doublets with binding energies of 458.5 eV and 464.6 eV, corresponding to Ti $2p_{3/2}$ and Ti $2p_{1/2}$, respectively, as shown in Figure 6c. Two additional minor peaks were detected at 459.1 and 463.0 eV, consistent with the presence of the Ti–C bond, confirming the robust adhesion of the RF layer to the surface of the $Na_2Ti_3O_7$ [54]. The C 1s spectrum of the RF layer (Figure 6d) is deconvoluted, revealing four distinct peaks centered at 284.2, 285.0, 285.7, and 286.1 eV which can be attributed to C–C, Ti–C, C–O, and C=O bonds, respectively [55,56]. The O 1s spectrum of the RF layer (Figure 6e) can be successfully deconvoluted with three discernible peaks at 530.6, 532.5, and 532.9 eV which are assigned to the C=O, Ti–O, and C–O groups, respectively [56,57]. The N 1s spectrum of the RF layer (Figure 6f) can also successfully deconvolute into two distinct peaks at 398.4 eV and 401.2.6 eV, corresponding to C-NH-C and C=N-C, respectively [58]. The HRXPS spectrum of Ag 3d (Figure 6g) can be observed at binding energies of 367.8 and 373.8 eV, corresponding to Ag $3d_{5/2}$ and Ag $3d_{3/2}$, respectively. The 6 kV binding energy difference between these peaks confirms the presence of an Ag^0 state [59].

SERS activity is intricately linked to the morphology, size, and density of Au and Ag nanoparticles, which collectively govern the efficiency and performance of SERS measurements [60,61]. This investigation assessed the SERS performance of the $Na_2Ti_3O_7$@RF@Ag heterostructures synthesized under various reaction conditions, using RhB as the target molecule. Figure 7a shows the SERS spectra of $Na_2Ti_3O_7$@RF@Ag heterostructures grown via different Ag-nanoparticle-deposition methods, such as the wet chemical method (only 0.15 mL of $AgNO_3$; 0.15 mL of $AgNO_3$ and 3 mL of L-ascorbic acid) and ion-sputtering method (Ag-ion-sputtering time of 90 s), which were immersed in the RhB solution (10^{-6} M) for 1h. The primary vibrational modes for the characteristic peaks of the RhB molecule are aromatic C–C stretching (1076 cm^{-1}), C-H in-plane bending (1197 cm^{-1}), C–H bending (1279 cm^{-1}), the stretching vibration of bridge C–C aromatic bonds (1360 cm^{-1}), aromatic C–C bending (1508 cm^{-1}), C–H stretching (1527 cm^{-1}), aromatic C-C bending, and C=C stretching vibration (1647 cm^{-1}), respectively [62,63]. This study chose a Raman peak at 1647 cm^{-1} as the reference point to assess SERS activity because it does not readily overlap with the SERS substrate or the solvent. The Raman intensity of RhB is significantly boosted in the presence of $Na_2Ti_3O_7$@RF@Ag heterostructures (0.15 mL of $AgNO_3$ and 3 mL of

L-ascorbic acid) compared to the $Na_2Ti_3O_7$@RF@Ag heterostructures (only 0.15 mL of $AgNO_3$) and the $Na_2Ti_3O_7$@RF@Ag heterostructure (Ag-ion-sputtering time of 90 s). The efficacy of the $Na_2Ti_3O_7$@RF@Ag heterostructures for RhB detection was assessed using the SERS enhancement factor (EF), determined by the formula $EF = I_{SERS} \times C_0/I_0 \times C_{SERS}$. Here, I_{SERS} and I_0 represent the SERS (with $Na_2Ti_3O_7$@RF@Ag heterostructures) and standard Raman intensities of RhB, while C_{SERS} and C_0 denote the RhB concentration on the $Na_2Ti_3O_7$@RF@Ag heterostructures (10^{-6} M) and bare Ti foil (10^{-4} M) [64,65]. The calculated maximum EF values for the RhB Raman band at 1647 cm^{-1} are 5.00×10^6 (0.15 mL $AgNO_3$), 1.09×10^7 (0.15 mL of $AgNO_3$ and 3 mL of L-ascorbic acid), and 2.88×10^6 (Ag-ion-sputtering time of 90 s), respectively. The $Na_2Ti_3O_7$@RF@Ag heterostructures (0.15 mL $AgNO_3$ and 3 mL L-ascorbic acid) are 2.18 and 3.78 times higher than the $Na_2Ti_3O_7$@RF@Ag heterostructures (0.15 mL of $AgNO_3$) and $Na_2Ti_3O_7$@RF@Ag heterostructures (Ag-ion-sputtering time of 90 s), respectively.
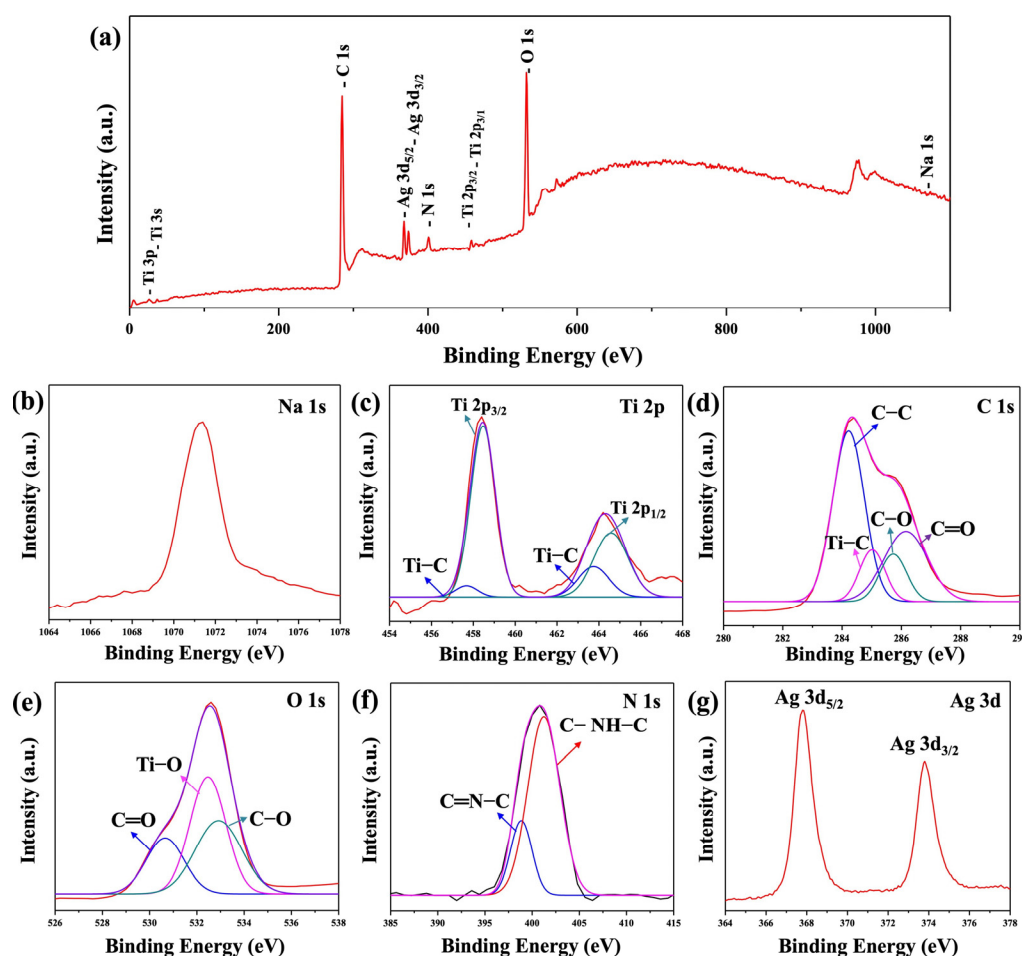

Figure 6. XPS spectra of the $Na_2Ti_3O_7$@RF@Ag heterostructures (0.15 mL Ag NO_3 and 3 mL L-ascorbic acid): (**a**) survey spectrum, (**b**) Na 1s, (**c**) Ti 2p, (**d**) C 1s, (**e**) O 1s, (**f**) N 1s, and (**g**) Ag 3d, respectively.

Figure 7b shows the SERS intensity of an RhB solution (10^{-6} M) at 1647 cm^{-1} obtained from $Na_2Ti_3O_7$@RF@Ag heterostructures grown using different volumes of $AgNO_3$. The most prominent Raman intensity is observed at 0.15 mL of $AgNO_3$. As the volume of $AgNO_3$ increases, there is a gradual decrease in the Raman intensity. As the SERS enhancement effect remained relatively low, this research introduced different volumes of L-ascorbic acid to expedite the formation and deposition of Ag nanoparticles, as shown in Figure 7c. The most prominent Raman signal is observed for 3 mL of L-ascorbic acid. This trend may be attributed to the more effective distribution of hot spots achieved with

3 mL of L-ascorbic acid, significantly enhancing Raman signal intensity. This result is consistent with previous FETEM observations. To confirm the effectiveness of the Ag nanoparticle preparation method employed in the wet chemical method compared to the ion-sputtering method, this study used the ion-sputtering method to deposit Ag nanoparticles onto $Na_2Ti_3O_7$@RF heterostructures at different times. Figure 7d reveals the SERS intensity of an RhB solution (10^{-6} M) at 1647 cm^{-1} obtained from $Na_2Ti_3O_7$@RF@Ag heterostructures grown using different Ag-ion-sputtering times. Hence, it can be determined that the most significant SERS enhancement effect was achieved with an ion-sputtering time of 90 s. This result is much lower than for $Na_2Ti_3O_7$@RF@Ag heterostructures prepared via wet chemical methods (0.15 mL of $AgNO_3$ and 3 mL of L-ascorbic acid). In order to understand the differences, $Na_2Ti_3O_7$@RF@Ag heterostructures (Ag-ion-sputtering time of 90 s) were further analyzed through FETEM. Figure 7e displays a FETEM image that depicts a size range of Ag nanoparticles, varying from approximately 3 to 21 nm. While the Ag nanoparticles are thoroughly dispersed within the $Na_2Ti_3O_7$@RF heterostructure, their size distribution appears irregular. This non-uniformity in size has consequences for the hot spot distribution on the heterostructure's surface, reducing its SERS enhancement effect [24,66]. Hence, the simplicity and remarkable efficiency of this study's Ag nanoparticle preparation method can be further validated.
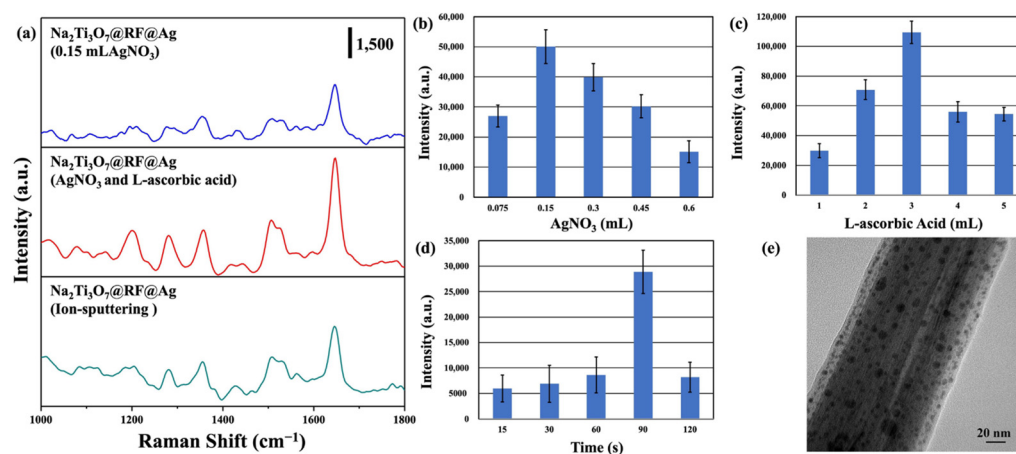

Figure 7. (**a**) SERS spectra of (10^{-6} M) RhB solution on $Na_2Ti_3O_7$@RF@Ag heterostructures (only 0.15 mL of $AgNO_3$), $Na_2Ti_3O_7$@RF@Ag heterostructures (0.15 mL of $AgNO_3$ and 3 mL of L-ascorbic acid), and $Na_2Ti_3O_7$@RF@Ag heterostructure (Ag-ion-sputtering time of 90 s). The SERS intensities of (10^{-6} M) RhB solution on $Na_2Ti_3O_7$@RF@Ag heterostructures at 1647 cm^{-1} under the different (**b**) $AgNO_3$ volumes, (**c**) L-ascorbic acid volumes, and (**d**) Ag-ion-sputtering times. (**e**) FETEM image of a $Na_2Ti_3O_7$@RF@Ag heterostructure (Ag-ion-sputtering time of 90 s).

The uniformity and reusability of SERS substrates are crucial factors in real-world SERS applications [25,47]. In order to assess the uniformity of the $Na_2Ti_3O_7$@RF@Ag heterostructures, ten random spots were chosen on the substrate loaded with RhB solution (10^{-6} M) for an SERS analysis. Figure 8a shows the SERS spectra of an RhB solution (10^{-6} M) acquired from these ten positions on the substrate. The Raman signals' peak positions and intensities exhibit remarkable uniformity across various locations on the the $Na_2Ti_3O_7$@RF@Ag heterostructures. This outcome further substantiates the effective enhancement of Raman signals achieved by the $Na_2Ti_3O_7$@RF@Ag heterostructures. The reusability of the $Na_2Ti_3O_7$@RF@Ag heterostructures is a pivotal concern in this study. In order to address this issue, RhB molecules were systematically eliminated from the $Na_2Ti_3O_7$@RF@Ag heterostructures using photocatalytic degradation facilitated by exposure to UV light for 1h. Figure 8b reveals the Raman spectra of $Na_2Ti_3O_7$@RF@Ag heterostructures initially immersed in an RhB solution with a 10^{-7} M concentration for 1 h. These spectra are presented before and after five consecutive UV light exposure cycles. These observations emphasize the remarkable reusability of the $Na_2Ti_3O_7$@RF@Ag

heterostructures, which consistently retain a comparable Raman signal strength even after undergoing five repeated cycles. This result reconfirms their enduring efficacy and suitability for practical applications. In addition, this occurrence can be attributed to the unique structural configuration of the $Na_2Ti_3O_7$@RF@Ag heterostructures, which provide an augmented quantity of hot spots and surface-active sites. As a result, $Na_2Ti_3O_7$@RF@Ag heterostructures exhibit remarkable SERS enhancement, excellent reproducibility, and sustained stability over an extended period.

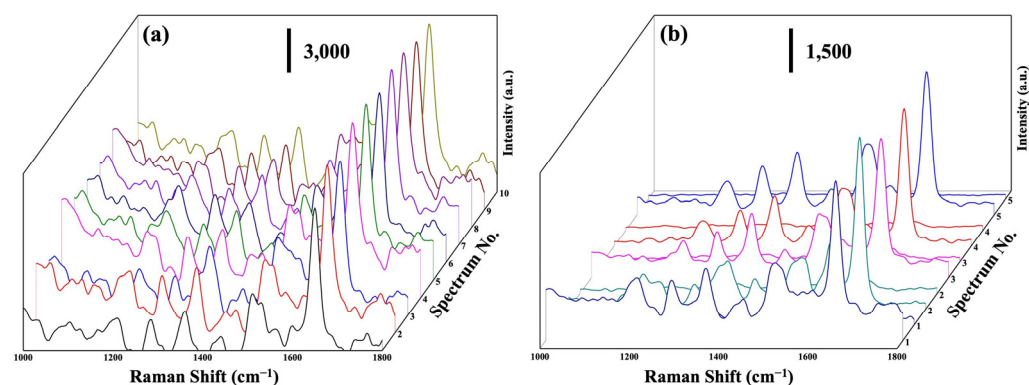**Figure 8.** (**a**) SERS spectra of a (10^{-6} M) RhB solution at 10 random points on $Na_2Ti_3O_7$@RF@Ag heterostructures. (**b**) SERS spectra of a (10^{-7} M) RhB solution on $Na_2Ti_3O_7$@RF@Ag heterostructures for the five cycles.

The SERS spectra were acquired for freshly synthesized SERS substrates after their immersion in different concentrations of RhB solution for 1 h, followed by air-drying. This assessment aimed to determine the low detection limit of the $Na_2Ti_3O_7$@RF@Ag heterostructures for RhB solutions. Figure 9a displays the SERS intensities of the $Na_2Ti_3O_7$@RF@Ag heterostructures at 1647 cm^{-1} over a concentration range from 10^{-6} M to 10^{-10} M of RhB solution. As the RhB concentration decreases, the SERS signal intensities at 1647 cm^{-1} gradually diminish. When the RhB solution concentration decreases below 10^{-10} M, the SERS signal at 1647 cm^{-1} becomes challenging to effectively detect for $Na_2Ti_3O_7$@RF@Ag heterostructures. Nevertheless, even at a concentration as low as 10^{-10} M, the SERS signal at 1647 cm^{-1} can still be reliably detected using $Na_2Ti_3O_7$@RF@Ag heterostructures. To ascertain the versatility of the $Na_2Ti_3O_7$@RF@Ag heterostructure across various organic dyes, this study investigated the SERS effect of different methylene blue (MB) concentrations. Figure 9b displays the SERS intensities of $Na_2Ti_3O_7$@RF@Ag heterostructures at 1623 cm^{-1} over a concentration range from 10^{-6} M to 10^{-10} M of MB solution. As the concentration of the MB solution drops below 10^{-10} M, effectively detecting the SERS signal at 1623 cm^{-1} becomes challenging for $Na_2Ti_3O_7$@RF@Ag heterostructures.

In order to evaluate the temporal stability of the $Na_2Ti_3O_7$@RF@Ag heterostructures, RhB and MB solutions, each with a concentration of 10^{-6} M, were analyzed after preparing the SERS substrate and storing it in the dark for different durations of 1, 8, 15, 22, and 29 days. Figure 9c,d present the SERS intensities of $Na_2Ti_3O_7$@RF@Ag heterostructures at 1647 cm^{-1} (RhB) and 1623 cm^{-1} (MB) for these different detection times, respectively. Remarkably, even after 29 days of storage, the intensities of the SERS signal at 1647 cm^{-1} (RhB) and 1623 cm^{-1} (MB) retain substantial levels of 60.4% and 48.9%, respectively. This result can verify that the $Na_2Ti_3O_7$@RF@Ag heterostructures exhibit long-term stability.

The primary absorption peak at 552 nm for RhB gradually diminishes as the duration of UV light irradiation increases [67,68]. Notably, there is no shift in the primary peak of RhB, indicating that the process primarily involves decomposing the benzene/heterocyclic rings [69]. In order to assess photocatalytic activity, a plot of (C/C_0) versus time is presented in Figure 10a. The photocatalytic efficiency values of various samples, including $Na_2Ti_3O_7$ nanowires, $Na_2Ti_3O_7$@RF heterostructures, $Na_2Ti_3O_7$@RF@Ag heterostructures (0.15 mL of $AgNO_3$ and 3 mL of L-ascorbic acid), and $Na_2Ti_3O_7$@RF@Ag heterostructures

(Ag-ion-sputtering of 90 s), are 76.3, 83.0, 86.5, and 79.7%, respectively. The Langmuir–Hinshelwood model is widely employed to assess the photodegradation kinetics of organic dyes in aqueous solutions. The reaction-rate constants (k) for different samples, including $Na_2Ti_3O_7$ nanowires, $Na_2Ti_3O_7$@RF heterostructures, $Na_2Ti_3O_7$@RF@Ag heterostructures (0.15 mL $AgNO_3$ and 3 mL L-ascorbic acid), and $Na_2Ti_3O_7$@RF@Ag heterostructures (Ag-ion-sputtering of 90 s), are determined to be 0.0079, 0.00966, 0.01112, and 0.00846 min^{-1}, respectively, as depicted in Figure 10b. These findings suggest that the $Na_2Ti_3O_7$@RF@Ag heterostructures (0.15 mL of $AgNO_3$ and 3 mL of L-ascorbic acid) exhibited approximately 1.4 and 1.3 times greater efficiency compared to $Na_2Ti_3O_7$ nanowires and $Na_2Ti_3O_7$@RF@Ag heterostructures (Ag-ion-sputtering of 90 s). The $Na_2Ti_3O_7$@RF@Ag heterostructures reveal exceptional efficiency as reusable photocatalysts for the photodecomposition of RhB solutions under UV light irradiation. This outcome can be ascribed to the heightened suppression of electron–hole pair recombination and the increased availability of surface-active sites.
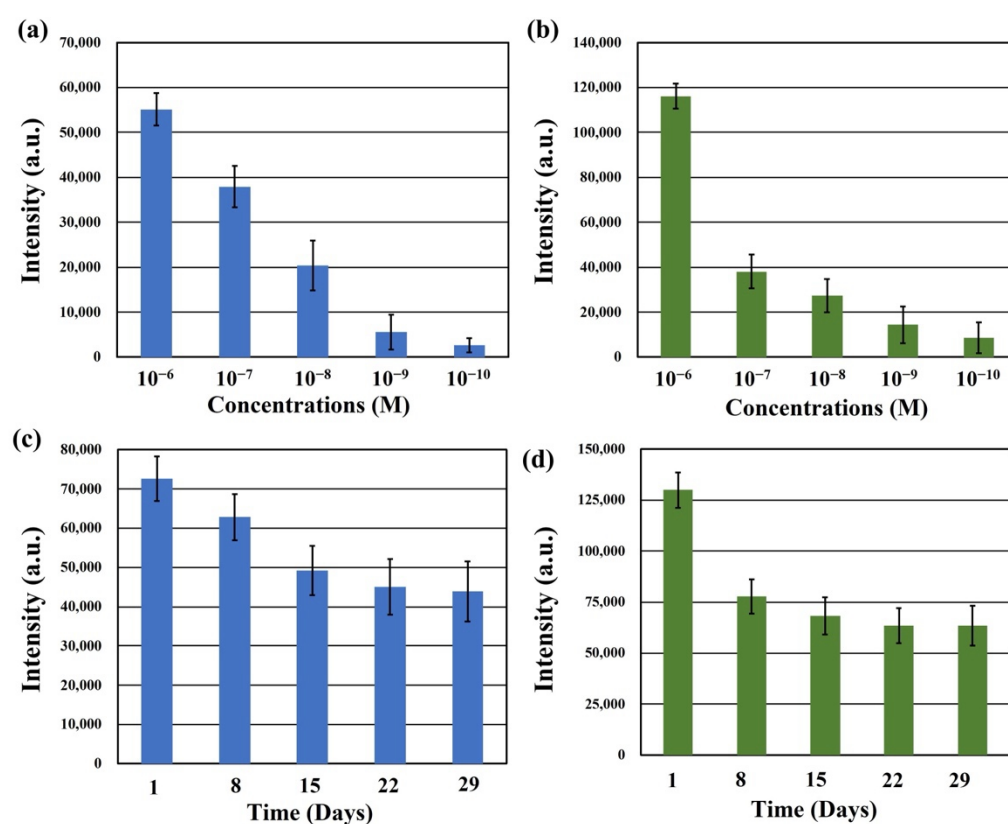

Figure 9. The SERS intensities of $Na_2Ti_3O_7$@RF@Ag heterostructures at (**a**) 1647 cm^{-1} (RhB) and (**b**) 1623 cm^{-1} (MB) under different concentrations of RhB and MB solutions, respectively. (**b**) The SERS intensities of $Na_2Ti_3O_7$@RF@Ag heterostructures at (**c**) 1647 cm^{-1} (RhB) and (**d**) 1623 cm^{-1} (MB) under different detection times.

The reusability of photocatalysts is of the utmost importance as it directly impacts their effectiveness in photocatalytic processes. In this study, an RhB solution with $Na_2Ti_3O_7$@RF@Ag heterostructures (0.15 mL of $AgNO_3$ and 3 mL of L-ascorbic acid) was subjected to UV light irradiation for 3 h. Subsequently, the substrate was thoroughly rinsed twice with copious amounts of de-ionized water in preparation for the next cycle of photodegradation. Over four cycles, the photocatalytic efficiency values of the $Na_2Ti_3O_7$@RF@Ag heterostructures on Ti foil were found to be 80.3, 80.4, 77.4, and 78.3, respectively, as depicted in Figure 11a. The results reveal that the $Na_2Ti_3O_7$@RF@Ag heterostructures exhibit superior reusability for decomposing the RhB solution. Furthermore, an XRD analysis of $Na_2Ti_3O_7$@RF@Ag heterostructures (0.15 mL of $AgNO_3$ and 3 mL of L-ascorbic acid) after undergoing four

cycles of recycling (Figure 11b) indicate no significant crystalline alterations, substantiating the enduring nature of the heterojunction. This analysis underscores the exceptional and sustained photocatalytic degradation efficiency of $Na_2Ti_3O_7$@RF@Ag heterostructures.
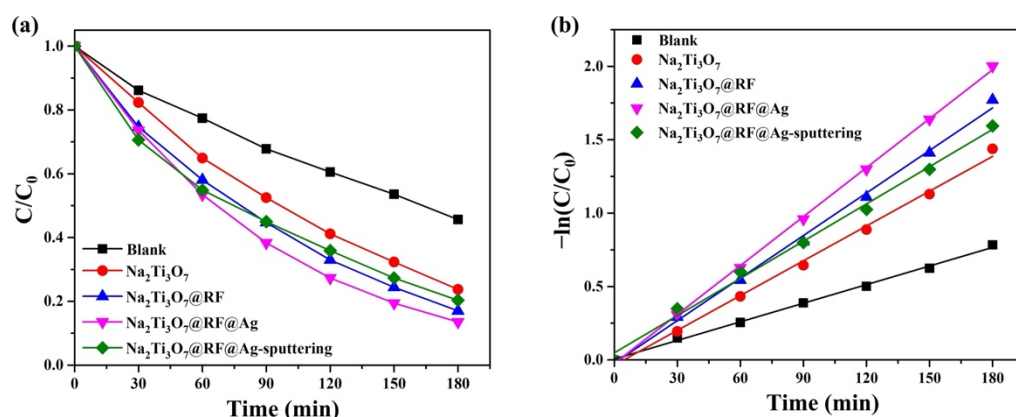

Figure 10. (**a**) Photocatalytic activities and (**b**) kinetic linear simulation curves of as-prepared photocatalysts under UV light irradiation.
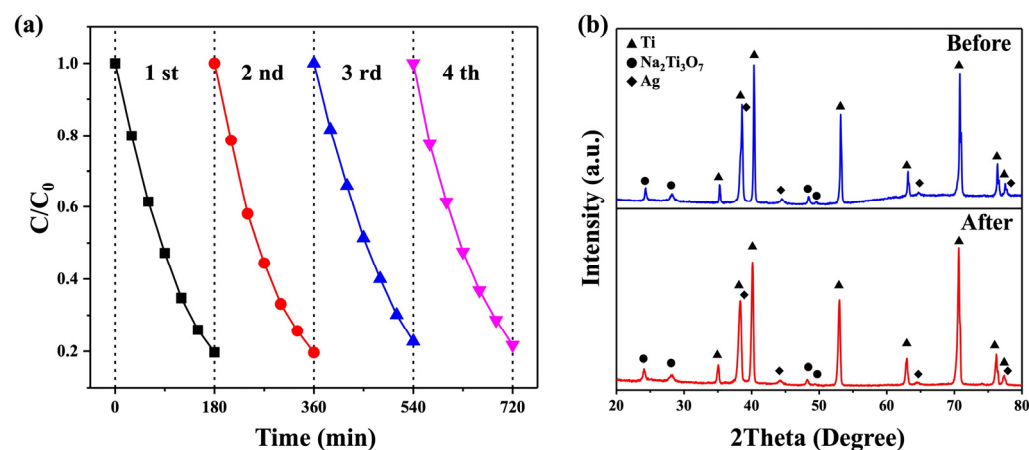

Figure 11. (**a**) The reusability of the $Na_2Ti_3O_7$@RF@Ag heterostructures under UV light irradiation. (**b**) XRD spectra of $Na_2Ti_3O_7$@RF@Ag heterostructures before cycling and after the fourth cycle.

3. Materials and Methods

3.1. Materials

A 0.25 mm thick titanium (Ti) foil (99.5%) was commercially sourced from Alfa Aesar (Haverhill, MA, USA). All chemicals used were obtained from commercial suppliers and were employed without the need for further purification. Specifically, hydrochloric acid (HCl, 37%), sodium hydroxide (NaOH, 97%), ethanol (C_2H_5OH, 99%), L-ascorbic acid ($C_6H_8O_6$, 99%), and rhodamine B (RhB, $C_{28}H_{31}ClN_2O_3$, 95%) were acquired from Sigma-Aldrich (Steinheim, Germany). (3-Aminopropyl)trimethoxysilane ($C_6H_{17}NO_3Si$, APTMS, 95%) was acquired from Acros (Renningen, Germany). Resorcinol ($C_6H_6O_2$, 99%), ammonium hydroxide (NH_4OH, 28%), methylene blue (MB, $C_{16}H_{18}ClN_3S$, 95%), and silver nitrate ($AgNO_3$, 99%) were obtained from Alfa Aesar (USA). A formaldehyde solution (CH_2O, 37%) was acquired from Merck (Darmstadt, Germany). De-ionized water with a resistivity exceeding 18.2 MΩ was used to prepare all solutions.

3.2. Syntheses of $Na_2Ti_3O_7$ Nanowires

A 0.25 mm thick titanium (Ti) foil was cut to the desired dimensions 0.5 cm × 0.5 cm or 1.5 cm × 2.5 cm. The substrate underwent ultrasonic treatment in ethanol and 1.0 M HCl for 10 min each, effectively removing organic contaminants and oxide layers. After each treatment, it was thoroughly rinsed with ethanol and dried using an air purge. Subsequently, the cleaned

substrate was placed in separate 50 mL Teflon-lined stainless-steel autoclaves containing a 0.375 M NaOH solution (20 mL) and heated to 220 °C for 5 h. Finally, the substrate was washed with de-ionized water and ethanol and dried via air purge.

3.3. Syntheses of $Na_2Ti_3O_7$@RF@Ag Heterostructures

The substrates featuring $Na_2Ti_3O_7$ nanowires underwent a surface hydrophilicity enhancement process by immersing them in a 50 mL ethanol solution containing 5 mM APTMS for 6 h at room temperature. Subsequently, the substrates were thoroughly rinsed with ethanol and de-ionized water and dried using an air purge. For the growth of the RF layer on the $Na_2Ti_3O_7$ nanowires, the substrates were placed in a 40 mL aqueous solution containing 16.37 mg of resorcinol, 0.0284 mL of NH_4OH, and 0.0444 mL of CH_2O. This mixture was vigorously stirred for 6 h at 50 °C. Next, the substrate was rinsed with ethanol thrice and dried at 60 °C for 2 h. To deposit Ag nanoparticles on the $Na_2Ti_3O_7$@RF heterostructures, the substrate was immersed in a 50 mL aqueous solution with different volumes of $AgNO_3$ (5 mM) and L-ascorbic acid (50 mM) under vigorous stirring for 1 h. Finally, the resulting substrate underwent several ethanol rinses and was dried at 60 °C for 2 h.

3.4. Characterization

The as-prepared SERS substrates underwent a comprehensive analysis to investigate their microstructures and elemental composition. Field-emission scanning electron microscopy (FESEM) was employed using a Hitachi S-4800 instrument (Tokyo, Japan). Field-emission transmission electron microscopy (FETEM) was also utilized with a JEOL JSM-2100F apparatus (Tokyo, Japan) equipped with energy-dispersive X-ray spectroscopy (EDS). X-ray diffraction (XRD) was performed using a Bruker (Billerica, MA, USA) D8 SSS instrument based in the United States to characterize the crystal structures of the as-prepared substrates. The chemical states of the elements within the $Na_2Ti_3O_7$@RF@Ag heterostructures were determined through X-ray photoelectron spectroscopy (XPS), conducted using a ULVAC-PHI PHI 5000 VersaProbe instrument (Chigasaki, Japan). Furthermore, SERS measurements were carried out using a micro-Raman identify spectrometer (MRI532S) provided by Protrustech in Taiwan. These measurements utilized an excitation wavelength of 532 nm, with a laser beam diameter of 3.3 mm and a resolution of 2.2 cm^{-1}.

3.5. SERS and Photocatalytic Measurement

For SERS measurement, a micro-Raman identify spectrometer with 532 nm excitation wavelength employed 1 mW laser power and 0.15 s detector integration time. The SERS properties of the $Na_2Ti_3O_7$@RF@Ag heterostructures were evaluated, immersing substrates in RhB solutions and drying them for 1 h at room temperature in the dark. For photocatalytic measurements, photocatalyst activity was assessed by degrading an RhB solution (0.08 mM) without pH adjustment under UV light (253.7 nm, 10 W, Philips, Amsterdam, The Netherlands) irradiation. Concentrations were measured with a DR/UV-Vis spectrometer (Hitachi U-2900, Tokyo, Japan), and efficiency was calculated as C/C_0, where C_0 and C represent initial and final RhB concentrations.

4. Conclusions

A 3D $Na_2Ti_3O_7$@RF@Ag heterostructure is synthesized through a multi-step process featuring $Na_2Ti_3O_7$ nanowire cores, an intermediate RF layer, and outer Ag nanoparticle sheaths. Initially, single-crystal $Na_2Ti_3O_7$ nanowires are grown directly on flexible Ti foil using a one-step hydrothermal technique. Subsequently, a two-step wet chemical process deposits the RF layer and Ag nanoparticles on the nanowires at a low temperature. By optimizing $AgNO_3$ and L-ascorbic acid concentrations, the resulting $Na_2Ti_3O_7$@RF@Ag heterostructures exhibit higher surface-enhanced Raman scattering (SERS) enhancement for detecting RhB molecules. The unique geometry of these heterostructures, providing numerous hot spots and surface-active sites, contributes to significant SERS enhancement,

remarkable reproducibility, and long-term stability. These Na$_2$Ti$_3$O$_7$@RF@Ag heterostructures efficiently serve as reusable photocatalysts for decomposing RhB solutions under UV light irradiation, benefitting from the enhanced inhibition of electron–hole pair recombination and an increased number of surface-active sites. This dual functionality highlights the versatility of Na$_2$Ti$_3$O$_7$@RF@Ag heterostructures, promising applications in environmental remediation and chemical sensing.

Author Contributions: Funding acquisition, methodology, project administration, resources, software, supervision, validation, writing—original draft, and writing—review and editing, Y.-C.C.; formal analysis, investigation, and data curation, I.-C.L.; funding acquisition and resources, N.-C.C., S.-E.J. and C.-M.C. All authors have read and agreed to the published version of the manuscript.

Institutional Review Board Statement: Not applicable.

Informed Consent Statement: Not applicable.

Data Availability Statement: Data are contained within the article.

Conflicts of Interest: Author Ning-Chien Chin was employed by the company "Antai Medical Care Corporation". The authors declare that this study received funding from "National Science and Technology Council, Taiwan" and "Taichung Veterans General Hospital, Taiwan". The funder was not involved in the study design, collection, analysis, interpretation of data, the writing of this article or the decision to submit it for publication.

References

1. Li, C.; Huang, Y.; Li, X.; Zhang, Y.; Chen, Q.; Ye, Z.; Alqarni, Z.; Bell, S.E.J.; Xu, Y. Towards practical and sustainable SERS: A review of recent developments in the construction of multifunctional enhancing substrates. *J. Mater. Chem. C* **2021**, *9*, 11517–11552. [CrossRef]

2. Mehmandoust, S.; Eskandari, V.; Karooby, E. A Review of Fabrication of DNA Origami Plasmonic Structures for the Development of Surface-Enhanced Raman Scattering (SERS) Platforms. *Plasmonics* **2023**. [CrossRef]

3. Ding, S.-Y.; You, E.-M.; Tian, Z.-Q.; Moskovits, M. Electromagnetic theories of surface-enhanced Raman spectroscopy. *Chem. Soc. Rev.* **2017**, *46*, 4042–4076. [CrossRef] [PubMed]

4. Sharma, B.; Frontiera, R.R.; Henry, A.-I.; Ringe, E.; Van Duyne, R.P. SERS: Materials, applications, and the future. *Mater. Today* **2012**, *15*, 16–25. [CrossRef]

5. Petryayeva, E.; Krull, U.J. Localized surface plasmon resonance: Nanostructures, bioassays and biosensing—A review. *Anal. Chim. Acta* **2011**, *706*, 8–24. [CrossRef]

6. Luo, S.-C.; Sivashanmugan, K.; Liao, J.-D.; Yao, C.-K.; Peng, H.-C. Nanofabricated SERS-active substrates for single-molecule to virus detection in vitro: A review. *Biosens. Bioelectron.* **2014**, *61*, 232–240. [CrossRef] [PubMed]

7. Reguera, J.; Langer, J.; Jimenez de Aberasturi, D.; Liz-Marzan, L.M. Anisotropic metal nanoparticles for surface enhanced Raman scattering. *Chem. Soc. Rev.* **2017**, *46*, 3866–3885. [CrossRef]

8. Mosier-Boss, P.A. Review of SERS Substrates for Chemical Sensing. *Nanomaterials* **2017**, *7*, 142. [CrossRef]

9. Eskandari, V.; Sahbafar, H.; Karooby, E.; Heris, M.H.; Mehmandoust, S.; Razmjoue, D.; Hadi, A. Surface-Enhanced Raman scattering (SERS) filter paper substrates decorated with silver nanoparticles for the detection of molecular vibrations of Acyclovir drug. *Spectrochim. Acta A Mol. Biomol. Spectrosc.* **2023**, *298*, 122762. [CrossRef]

10. Feng, J.; Chen, L.; Xia, Y.; Xing, J.; Li, Z.; Qian, Q.; Wang, Y.; Wu, A.; Zeng, L.; Zhou, Y. Bioconjugation of Gold Nanobipyramids for SERS Detection and Targeted Photothermal Therapy in Breast Cancer. *ACS Biomater. Sci. Eng.* **2017**, *3*, 608–618. [CrossRef]

11. Sivanesan, A.; Adamkiewicz, W.; Kalaivani, G.; Kamińska, A.; Waluk, J.; Hołyst, R.; Izake, E.L. Electrochemical pathway for the quantification of SERS enhancement factor. *Electrochem. Commun.* **2014**, *49*, 103–106. [CrossRef]

12. Pilot, R.; Signorini, R.; Durante, C.; Orian, L.; Bhamidipati, M.; Fabris, L. A Review on Surface-Enhanced Raman Scattering. *Biosensors* **2019**, *9*, 57. [CrossRef] [PubMed]

13. Fan, M.; Andrade, G.F.S.; Brolo, A.G. A review on recent advances in the applications of surface-enhanced Raman scattering in analytical chemistry. *Anal. Chim. Acta* **2020**, *1097*, 1–29. [CrossRef] [PubMed]

14. Liu, H.; Liu, Y.; Zhou, T.; Zhou, P.; Li, J.; Deng, A. Ultrasensitive and Specific Detection of Anticancer Drug 5-Fluorouracil in Blood Samples by a Surface-Enhanced Raman Scattering (SERS)-Based Lateral Flow Immunochromatographic Assay. *Molecules* **2022**, *27*, 4019. [CrossRef] [PubMed]

15. Chang, Y.-C.; Lin, J.-C.; Chou, C.-M. H2Ti3O7 nanowires as a high-performance photocatalytic and surface-enhanced Raman scattering substrate. *J. Photochem. Photobiol. A Chem.* **2020**, *400*, 112666. [CrossRef]

16. Tereshchenko, A.; Bechelany, M.; Viter, R.; Khranovskyy, V.; Smyntyna, V.; Starodub, N.; Yakimova, R. Optical biosensors based on ZnO nanostructures: Advantages and perspectives. A review. *Sens. Actuators B Chem.* **2016**, *229*, 664–677. [CrossRef]

17. Chang, T.-H.; Chang, Y.-C.; Wu, S.-H. Ag nanoparticles decorated ZnO: Al nanoneedles as a high-performance surface-enhanced Raman scattering substrate. *J. Alloys Compd.* **2020**, *843*, 156044. [CrossRef]

18. ÇElİK, Y.; Kurt, A. Three dimensional porous Expanded Graphite/Silver Nanoparticles nanocomposite platform as a SERS substrate. *Appl. Surf. Sci.* **2021**, *568*, 150946. [CrossRef]

19. La Ngoc Tran, N.; Van Hoang, D.; Tuan Thanh Pham, A.; Tran Truc Phuong, N.; Xuan Dat Mai, N.; Chi, T.T.K.; Hien, B.T.T.; Bach Phan, T.; Tran, N.H.T. Novel composites of nano-metal–organic frameworks (IRMOF-3) and silver nanoparticles for the ultra-sensitive performance of SERS sensing and optical fiber modes. *J. Sci. Adv. Mater. Devices* **2023**, *8*, 100584. [CrossRef]

20. Karooby, E.; Sahbafar, H.; Heris, M.H.; Hadi, A.; Eskandari, V. Identification of Low Concentrations of Flucytosine Drug Using a Surface-Enhanced Raman Scattering (SERS)-Active Filter Paper Substrate. *Plasmonics* **2023**. [CrossRef]

21. Wei, W.; Du, Y.; Zhang, L.; Yang, Y.; Gao, Y. Improving SERS hot spots for on-site pesticide detection by combining silver nanoparticles with nanowires. *J. Mater. Chem. C* **2018**, *6*, 8793–8803. [CrossRef]

22. Chou, C.-M.; Chang, T.-T.; Chen, C.-Y.; Chang, Y.-C. Constructing Er-Doped ZnO/CuS/Au Core-Shell Nanowires with Enhanced Photocatalytic and SERS Properties. *Catalysts* **2021**, *11*, 1347. [CrossRef]

23. Chang, Y.-C.; Wu, S.-H. Bi-functional Al-doped ZnO@SnO2 heteronanowires as efficient substrates for improving photocatalytic and SERS performance. *J. Ind. Eng. Chem.* **2019**, *76*, 333–343. [CrossRef]

24. Zhao, X.-Y.; Wang, G.; Hong, M. Hybrid structures of Fe3O4 and Ag nanoparticles on Si nanopillar arrays substrate for SERS applications. *Mater. Chem. Phys.* **2018**, *214*, 377–382. [CrossRef]

25. Chang, T.-H.; Chuang, K.-W.; Chang, Y.-C. Ag/Ga-doped ZnO/pyramidal silicon as a multifunctional surface-enhanced Raman scattering substrate. *J. Alloys Compd.* **2022**, *893*, 162288. [CrossRef]

26. Li, Z.; Han, K.; Zhang, A.; Wang, T.; Yan, Z.; Ding, Z.; Shen, Y.; Zhang, M.; Zhang, W. Honeycomb-like AgNPs@TiO2 array SERS sensor for the quantification of micro/nanoplastics in the environmental water samples. *Talanta* **2024**, *266*, 125070. [CrossRef]

27. Xie, Z.; Zhao, F.; Zou, S.; Zhu, F.; Zhang, Z.; Wang, W. TiO2 nanorod arrays decorated with Au nanoparticles as sensitive and recyclable SERS substrates. *J. Alloys Compd.* **2021**, *861*, 157999. [CrossRef]

28. Chen, L.; Jin, Y.; Guo, S.; Park, E.; Xie, Y.; Jung, Y.M. Ag decoration on Na2Ti3O7 nanowires for improved SERS and PHE performance. *Nanoscale* **2023**, *15*, 16287–16298. [CrossRef]

29. Vattikuti, S.V.P.; Devarayapalli, K.C.; Dang, N.N.; Shim, J. 1D/1D Na2Ti3O7/SWCNTs electrode for split-cell-type asymmetric supercapacitor device. *Ceram. Int.* **2021**, *47*, 11602–11610. [CrossRef]

30. Rudola, A.; Saravanan, K.; Mason, C.W.; Balaya, P. Na2Ti3O7: An intercalation based anode for sodium-ion battery applications. *J. Mater. Chem. A* **2013**, *1*, 2653–2662. [CrossRef]

31. Silva, F.L.R.e.; Filho, A.A.A.; da Silva, M.B.; Balzuweit, K.; Bantignies, J.-L.; Caetano, E.W.S.; Moreira, R.L.; Freire, V.N.; Righi, A. Polarized Raman, FTIR, and DFT study of Na2Ti3O7 microcrystals. *J. Raman Spectrosc.* **2018**, *49*, 538–548. [CrossRef]

32. Dong, J.; Jiang, Y.; Wang, R.; Wei, Q.; An, Q.; Zhang, X. Review and prospects on the low-voltage Na2Ti3O7 anode materials for sodium-ion batteries. *J. Energy Chem.* **2023**, *88*, 446–460. [CrossRef]

33. Teshima, K.; Lee, S.; Murakoshi, S.; Suzuki, S.; Kiyohara, M.; Yubuta, K.; Shishido, T.; Endo, M.; Oishi, S. A Unique Three-Dimensional Photocatalytic Structure Consisting of Highly Crystalline Na2Ti3O7 Whiskers Grown from a NaCl Flux. *Cryst. Growth Des.* **2010**, *10*, 2533–2540. [CrossRef]

34. Xu, C.-Y.; Wu, J.; Zhang, P.; Hu, S.-P.; Cui, J.-X.; Wang, Z.-Q.; Huang, Y.-D.; Zhen, L. Molten salt synthesis of Na2Ti3O7 and Na2Ti6O13 one-dimensional nanostructures and their photocatalytic and humidity sensing properties. *CrystEngComm* **2013**, *15*, 3448–3454. [CrossRef]

35. Chang, Y.-C.; Lin, J.-C.; Wu, S.-H. One-step growth of Na2Ti3O7 nanorods for enhanced photocatalytic activities and recyclability. *J. Alloys Compd.* **2018**, *749*, 955–960. [CrossRef]

36. Liu, D.-S.; Jin, F.; Huang, A.; Sun, X.; Su, H.; Yang, Y.; Zhang, Y.; Rui, X.; Geng, H.; Li, C.C. Phosphorus-Doping-Induced Surface Vacancies of 3D Na2Ti3O7 Nanowire Arrays Enabling High-Rate and Long-Life Sodium Storage. *Chem. Eur. J.* **2019**, *25*, 14881–14889. [CrossRef] [PubMed]

37. De, P.; Mandal, D.; Biswas, S.; Kumar, A.; Priya, S.; Dubey, B.K.; Srivastava, A.K.; Chandra, A. Tuning Na2Ti3O7 Nanostructures for Tailoring High-Performance Na-Ion Supercapacitors. *Energy Fuels* **2023**, *37*, 5595–5606. [CrossRef]

38. Li, H.; Huang, Y.; Liu, J.; Duan, H. Hydrothermally synthesized titanate nanomaterials for the removal of heavy metals and radionuclides from water: A review. *Chemosphere* **2021**, *282*, 131046. [CrossRef]

39. Wang, W.; He, S.-a.; Cui, Z.; Liu, Q.; Yuen, M.F.; Zhu, J.; Wang, H.; Gao, M.; Luo, W.; Hu, J.; et al. Boosting Charge Transfer Via Heterostructure Engineering of Ti2CTx/Na2Ti3O7 Nanobelts Array for Superior Sodium Storage Performance. *Small* **2022**, *18*, 2203948. [CrossRef]

40. Du, K.; Rudola, A.; Balaya, P. Investigations of Thermal Stability and Solid Electrolyte Interphase on $Na_2Ti_3O_7$/C as a Non-carbonaceous Anode Material for Sodium Storage Using Non-flammable Ether-based Electrolyte. *ACS Appl. Mater. Interfaces* **2021**, *13*, 11732–11740. [CrossRef]

41. Basilio, L.A.L.; Xavier, F.; Sales, J.C.C.; Andrade, J.C.S.; Anglada- Rivera, J.; Aguilera, L.; Silva, R.S.; Rodriguez-Hernandez, J.; Pérez de la Cruz, J.; Leyet, Y. Fast synthesis of $Na_2Ti_3O_7$ system synthesized by microwave-assisted hydrothermal method: Electrical properties. *Ceram. Int.* **2020**, *46*, 23834–23839. [CrossRef]

42. Cui, S.; Dai, Z.; Tian, Q.; Liu, J.; Xiao, X.; Jiang, C.; Wu, W.; Roy, V.A.L. Wetting properties and SERS applications of ZnO/Ag nanowire arrays patterned by a screen printing method. *J. Mater. Chem. C* **2016**, *4*, 6371–6379. [CrossRef]

43. Liu, C.; Xu, X.; Wang, C.; Qiu, G.; Ye, W.; Li, Y.; Wang, D. ZnO/Ag nanorods as a prominent SERS substrate contributed by synergistic charge transfer effect for simultaneous detection of oral antidiabetic drugs pioglitazone and phenformin. *Sens. Actuators B Chem.* **2020**, *307*, 127634. [CrossRef]

44. Chang, T.-H.; Chang, Y.-C.; Chen, C.-M.; Chuang, K.-W.; Chou, C.-M. A facile method to directly deposit the large-scale Ag nanoparticles on a silicon substrate for sensitive, uniform, reproducible and stable SERS substrate. *J. Alloys Compd.* **2019**, *782*, 887–892. [CrossRef]

45. Liao, W.; Liu, K.; Chen, Y.; Hu, J.; Gan, Y. Au–Ag bimetallic nanoparticles decorated silicon nanowires with fixed and dynamic hot spots for ultrasensitive 3D SERS sensing. *J. Alloys Compd.* **2021**, *868*, 159136. [CrossRef]

46. Zhao, X.; Zhang, M.; Sun, X.; Li, X.; Li, J.-g. Comprehensive understanding of the formation process on monodisperse resorcinol-formaldehyde polymer and carbon spheres and their use as substrates for surface-enhanced Raman spectroscopy. *Appl. Surf. Sci.* **2020**, *506*, 144591. [CrossRef]

47. Chang, T.-H.; Di, H.-W.; Chang, Y.-C.; Chou, C.-M. Ag Nanoparticles Decorated CuO@RF Core-Shell Nanowires for High-Performance Surface-Enhanced Raman Spectroscopy Application. *Molecules* **2022**, *27*, 8460. [CrossRef]

48. Yang, T.; Liu, J.; Zheng, Y.; Monteiro, M.J.; Qiao, S.Z. Facile Fabrication of Core–Shell-Structured Ag@Carbon and Mesoporous Yolk–Shell-Structured Ag@Carbon@Silica by an Extended Stöber Method. *Chem. Eur. J.* **2013**, *19*, 6942–6945. [CrossRef]

49. Cao, H.-L.; Liu, C.; Cai, F.-Y.; Qiao, X.-X.; Dichiara, A.B.; Tian, C.; Lü, J. In situ immobilization of ultra-fine Ag NPs onto magnetic Ag@RF@Fe_3O_4 core-satellite nanocomposites for the rapid catalytic reduction of nitrophenols. *Water Res.* **2020**, *179*, 115882. [CrossRef]

50. Yang, P.; Xu, Y.; Chen, L.; Wang, X.; Zhang, Q. One-Pot Synthesis of Monodisperse Noble Metal @ Resorcinol-Formaldehyde (M@RF) and M@Carbon Core–Shell Nanostructure and Their Catalytic Applications. *Langmuir* **2015**, *31*, 11701–11708. [CrossRef]

51. Miao, Z.; Zhao, Y.; Luan, Y.; Du, X. Synthesis of dendritic porous silica nanospheres coated by polymer layer with well-dispersed ultrasmall Pt nanoparticles. *Colloids Surf. A Physicochem. Eng. Asp.* **2021**, *618*, 126407. [CrossRef]

52. Panda, M.R.; Kathribail, A.R.; Modak, B.; Sau, S.; Dutta, D.P.; Mitra, S. Electrochemical properties of biomass-derived carbon and its composite along with $Na_2Ti_3O_7$ as potential high-performance anodes for Na-ion and Li-ion batteries. *Electrochim. Acta* **2021**, *392*, 139026. [CrossRef]

53. Gao, L.; Ma, Y.; Cao, M. Self-supported Se-doped $Na_2Ti_3O_7$ arrays for high performance sodium ion batteries. *Int. J. Hydrogen Energy* **2023**, *49*, 1–10. [CrossRef]

54. Akhavan, O.; Ghaderi, E. Photocatalytic Reduction of Graphene Oxide Nanosheets on TiO_2 Thin Film for Photoinactivation of Bacteria in Solar Light Irradiation. *J. Phys. Chem. C* **2009**, *113*, 20214–20220. [CrossRef]

55. Shiraishi, Y.; Takii, T.; Hagi, T.; Mori, S.; Kofuji, Y.; Kitagawa, Y.; Tanaka, S.; Ichikawa, S.; Hirai, T. Resorcinol–formaldehyde resins as metal-free semiconductor photocatalysts for solar-to-hydrogen peroxide energy conversion. *Nat. Mater.* **2019**, *18*, 985–993. [CrossRef] [PubMed]

56. Henn, F.; Tannert, R. Hydrophobization of Monolithic Resorcinol-Formaldehyde Xerogels by Means of Silylation. *Gels* **2022**, *8*, 304. [CrossRef]

57. Zhang, G.; Ni, C.; Liu, L.; Zhao, G.; Fina, F.; Irvine, J.T.S. Macro-mesoporous resorcinol–formaldehyde polymer resins as amorphous metal-free visible light photocatalysts. *J. Mater. Chem. A* **2015**, *3*, 15413–15419. [CrossRef]

58. Su, P.; Zhang, J.; Zhou, Y.; Wei, Z.; Zhao, S.; Yang, B.; Zhao, X.; Chen, J. Efficient photocatalytic production of hydrogen peroxide by Z-scheme resorcinol-formaldehyde resin/g-C3N4 heterostructure under visible light. *Chem. Eng. J.* **2023**, *454*, 140504. [CrossRef]

59. Kiran, J.U.; Roners, J.P.; Mathew, S. XPS and thermal studies of silver doped SiO2 matrices for plasmonic applications. *Mater. Today Proc.* **2020**, *33*, 1263–1267. [CrossRef]

60. Shameer, P.M.; Vijai Anand, K.; Columbus, S.; Alawadhi, H.; Daoudi, K.; Gaidi, M.; Govindaraju, K. Highly efficient, multiplexed SERS sensing of para-aminobenzoic acid using reusable silver nanoarrays for environmental monitoring. *Mater. Sci. Eng. B* **2023**, *295*, 116576. [CrossRef]

61. Chang, T.-H.; Liu, Y.-T.; Chang, Y.-C.; Lo, A.-Y. Fabrication of Three-Dimensional ZnO: Ga@ITO@Ag SERS-Active Substrate for Sensitive and Repeatable Detectability. *Nanomaterials* **2023**, *13*, 163. [CrossRef] [PubMed]

62. Godad, S.P.; Kamal, S. Multifunctional Ag_2CO_3 microrods as SERS-active substrate for the detection and degradation of Rhodamine B dye. *Spectrochim. Acta A Mol. Biomol. Spectrosc.* **2021**, *263*, 120176. [CrossRef] [PubMed]

63. Chen, X.; Zhu, L.; Ma, Z.; Wang, M.; Zhao, R.; Zou, Y.; Fan, Y. Ag Nanoparticles Decorated ZnO Nanorods as Multifunctional SERS Substrates for Ultrasensitive Detection and Catalytic Degradation of Rhodamine B. *Nanomaterials* **2022**, *12*, 2394. [CrossRef] [PubMed]

64. Dai, Q.; Li, L.; Wang, C.; Lv, C.; Su, Z.; Chai, F. Fabrication of a Flowerlike Ag Microsphere Film with Applications in Catalysis and as a SERS Substrate. *Eur. J. Inorg. Chem.* **2018**, *2018*, 2835–2840. [CrossRef]

65. Ma, Y.; Yang, L.; Yang, Y.; Peng, Y.; Wei, Y.; Huang, Z. Multifunctional Ag-decorated g-C3N4 nanosheets as recyclable SERS substrates for CV and RhB detection. *RSC Adv.* **2018**, *8*, 22095–22102. [CrossRef] [PubMed]

66. Zhao, X.; Zhang, W.; Peng, C.; Liang, Y.; Wang, W. Sensitive surface-enhanced Raman scattering of TiO_2/Ag nanowires induced by photogenerated charge transfer. *J. Colloid Interface Sci.* **2017**, *507*, 370–377. [CrossRef]

67. Qi, Y.; Zhao, J.; Wang, H.; Yan, M.; Guo, T. Structural engineering of BiOBr nanosheets for boosted photodegradation performance toward rhodamine B. *RSC Adv.* **2022**, *12*, 8908–8917. [CrossRef]

68. Song, L.; Li, Y.; He, P.; Zhang, S.; Wu, X.; Fang, S.; Shan, J.; Sun, D. Synthesis and sonocatalytic property of rod-shape $Sr(OH)_2 \cdot 8H_2O$. *Ultrason. Sonochem.* **2014**, *21*, 1318–1324. [CrossRef]

69. Panthi, G.; Gyawali, K.R.; Park, M. Towards the Enhancement in Photocatalytic Performance of Ag_3PO_4 Nanoparticles through Sulfate Doping and Anchoring on Electrospun Nanofibers. *Nanomaterials* **2020**, *10*, 929. [CrossRef]